A&A, 688, A35 (2024)
https://doi.org/10.1051/0004-6361/202347082

Astronomy & Astrophysics

Thermal and magnetic field structure of near-equatorial coronal holes

M. Hegde and K. M. Hiremath

Indian Institute of Astrophysics (IIA), Koramangala, Bengaluru, India
e-mail: manjunath@iiap.res.in; hiremath@iiap.res.in

Received 2 June 2023 / Accepted 1 March 2024

ABSTRACT

Context. Coronal holes are low-density and unipolar magnetic field structures in the solar corona that trigger geomagnetic disturbances on the Earth. Hence, it is important to understand the genesis and evolutionary behavior of these coronal activity features during their passage across the solar disk.
Aims. We study the day-to-day latitudinal variations of thermal and magnetic field structures of near-equatorial coronal holes. For this purpose, eight years of full-disk SOHO/EIT 195 Å calibrated images were used.
Methods. Using the response curves of the SOHO/EIT channels and assuming thermodynamic equilibrium, we estimated the temperature structure of coronal holes. From the latitudinal variation in the magnetic pressure, we inferred the magnitude of the magnetic field structure of coronal holes.
Results. Except for the temperature T, we find that the variations in the average photon flux F, in the radiative energy E, in the area A, and in the magnitude of the magnetic field structure $|B|$ of coronal holes depend on latitude. The typical average values of the estimated physical parameters are $A \sim 3.8(\pm0.5) \times 10^{20}$ cm^2, $F \sim 2.3(\pm0.2) \times 10^{13}$ photons cm^{-2} s^{-1}, $E \sim 2.32(\pm0.5) \times 10^3$ ergs cm^{-2} s^{-1}, $T \sim 0.94(\pm0.1) \times 10^6$ K and $|B| \sim 0.01(\pm0.001)$ G.
Conclusions. When coronal holes are anchored in the convection zone, these activity features would be expected to rotate differentially. The thermal wind balance and isorotation of coronal holes with the solar plasma therefore implies a measurable temperature difference between the equator and the two poles. Contrary to this fact, the variation in the thermal structure of near-equatorial coronal holes is independent of latitude, which leads to the conclusion that coronal holes must rotate rigidly and are likely to be initially anchored below the tachocline. This confirms our previous study.

Key words. methods: observational – methods: statistical

1. Introduction

Coronal holes (CHs) have unipolar magnetic field structures (Harvey & Sheeley 1979; Harvey et al. 1982) and are the lowest-density plasma structures. They are mainly detected in either UV or X-ray radiations of the solar atmosphere. These structures are associated with rapidly expanding magnetic fields and with the acceleration of the high-speed solar wind (Krieger et al. 1973; Neupert & Pizzo 1974; Nolte et al. 1976; Zirker 1977; Wang 2009; Wiegelmann et al. 2014; Cranmer 2009, and references therein). Possible links of the sunspot activity with the Earth's atmosphere and climate are well recorded in the literature (Hiremath 2009; Hiremath & Mandi 2004, and references therein). Recently, evidence is building up that coronal holes also trigger responses in the Earth's upper atmosphere and magnetosphere (Soon et al. 2000; Lei et al. 2008; Shugai et al 2009; Sojka et al. 2009; Choi et al. 2009; Tulasi Ram et al. 2010; Krista et al. 2011; Verbanac et al. 2011; Fathy et al.2014; Machiya & Akasofu 2014). Hiremath et al. (2015) concluded that in addition to the influence of sunspots, the radiative emission of coronal holes also triggers and maintains the Indian monsoon rainfall. For this purpose, the radiative flux and energy of the CH at 1 AU must be estimated during their evolution passage across the solar disk. It will be very useful to estimate the various physical parameters of CHs for modeling the observed physical parameters of different instruments, including Aditya Solar wind Particle Experiment (ASPEX; Goyal et al. 2018), Plasma Analyser Package for Aditya (PAPA), and the magnetometer on board Aditya-L1 (Tripathi et al. 2023). Keeping these main objectives in mind, we estimated the thermal structure of CH such as radiative flux, energy, and hence temperature at the Sun and at the Lagrangian point L_1 near 1 AU based on SOHO/EIT 195 Å calibrated images.

The dynamics such as the rotation rates (Hiremath & Hegde 2013, and references therein) and in situ plasma conditions of the CH are also of considerable interest for the solar community because the fast solar wind most likely originates in these regions (Stucki et al. 2002; Hegde et al. 2015). Ion temperatures in a polar coronal hole were estimated from line width measurements (Tu et al. 1998). The center-to-limb variation of the radiance of the transition region and coronal lines was obtained by Wilhelm et al. (1998). Doppler-shift measurements of the C II, O VI, and Ne VIII lines were obtained by Warren et al. (1997). Peter & Judge (1999) also studied these and a few other lines and found that the transition from redshift to blueshift occurs at electron temperatures of about 5×10^5 K. The analysis of SXT/Yohkoh images by Hara et al. (1996) showed that the estimated temperature structure ($1.8-2.4 \times 10^6$ K) in CH is of same order as the temperature in the ambient medium. Mogilevsky et al. (1997) also arrived at a similar conclusion. From the analysis of Big Bear Solar Observatory magnetograms and SOHO EIT images, Zhang et al. (2007) concluded that the

temperature of a coronal hole and the temperature of the ambient medium are not entirely different.

In recent years, space-based observations such as the Yohkoh and SOHO missions have been extensively used to estimate the temperature structure of CH (Hara et al. 1994; Moses et al. 1997). One physical parameter that senses the thermal structure of CH is the electron temperature. It is estimated by different spectroscopic methods. A detailed assessment of observations of CHs, and the deduced temperatures were published by Habbal et al. (1993). We also refer to the detailed review of the estimation of the coronal hole temperature by Habbal (1996) and Wilhelm (2012). The electron temperatures of CH can be measured with the help of the magnesium line ratio of a temperature-sensitive pair (see Wilhelm 2006). With the assumption that the density and temperature of the gas from which the spectral lines form are constant along the line of sight, Habbal et al. (1993) estimated the temperature structure of CH. Using two SOHO spectrometers, CDS and SUMER, the electron temperature of CH was measured as a function of height above the limb in a polar coronal hole (David et al. 1998; Wilhelm et al. 1998). Doschek & Laming (2000) found that the increase in the emission-line ratio of the polar coronal hole is primarily due to the increase in the electron temperature with height. Marsch et al. (2000) found that the hydrogen temperature increased only slightly from 1×10^5 to 2×10^5 K in the height range from 12 000 to 18 000 km. Stucki et al. (2000) reported that with increasing formation temperature, the spectral lines show an increasingly stronger blueshift in coronal holes on average relative to the quiet Sun at equal heliospheric angles. Furthermore, Xia et al. (2004) reported that the bases of coronal holes seen in chromospheric spectral lines with relatively low formation temperatures displayed properties similar to those of normal quiet-Sun regions. More recently, Wilhelm (2006, 2012) suggested that in a polar coronal hole, the electron temperature in plumes was estimated to be $\sim 8 \times 10^5$ K and, $\sim 1.13 \times 10^6$ K in the inter plume regions, at a height of 45 Mm above the limb.

From the silicon and iron coronal lines, Doschek & Feldman (1977) concluded that CH temperature must be lower than 1 MK. From the jets of coronal holes, Nisticò et al. (2011) computed the electron temperature of a CH by the filter ratio method at 171 Å and 195 Å and estimated a temperature structure with a magnitude in the range of ~0.18−1.3 MK. By using two lines, Mg IX (368 Å) and Mg X (625 Å), and with a similar line ratio technique, Doyle et al. (2010) derived the different coronal hole temperature structures during solar maximum (~1.04 MK) and minimum (~0.82 MK). The extreme-UV (EUV; Fe XV at 284 Å) and radio (at 169 and 408 MHz) observations of Chiuderi Drago et al. (1977) suggested that a CH consists of hot (10% of the CH surface with $\sim 2 \times 10^6$ K) and cold ($\sim 0.8 \times 10^6$ K) regions to explain observations of both the EUV and radio coronal hole temperature structures. From the analysis of EUV (SOHO/CDS) and radio emission (164−410 MHz obtained with the Nancay Radioheliograph, France), and with a model, Chiuderi Drago et al. (1999) estimated the CH temperature structure to be $\sim 9 \times 10^5$ K. From the spectroscopic diagnostics of Mg VIII (430.47 Å and 436.62 Å) ion, observed by Sky laboratory space probe, Dwivedi & Mohan (1995) estimated the coronal hole electron temperature to be $\sim 8 \times 10^5$ K. Dwivedi et al. (2000) estimated based on SUMER observations a CH temperature of $\sim (6.5-7.5) \times 10^5$ K. Observations of the Lyα, Mg X (625 Å), and O VI (1038 Å) spectral lines with the UVCS instrument on board SOHO from 1.35−2.1 $R_\odot$ yield that the proton temperature of a CH slowly increases between 1.35 and 2.7 $R_\odot$ and does not exceed 3×10^6 K in this region (Esser et al. 1999).

In most of the studies cited above, the estimated electron temperature along the slit of the observations over the region of a CH does not represent the temperature structure of the whole CH. However, by considering the whole CH, we present a simple method for estimating the average radiative flux, energy, and temperature structure of a CH at the Sun and near Earth.

As the speed of solar wind due to coronal hole is directly proportional to the area (Borisenko & Bogachev 2023; Hegde et al. 2015; Rotter et al. 2012; Karachik & Pevtsov 2011; Abramenko et al. 2009; Shugai et al. 2009; Vršnak et al. 2007; Nolte et al. 1976), it is interesting to examine how these parameters vary during the evolution of a coronal hole. To be specific, for example, as the Earth's ionosphere responds (Gulyaeva & Gulyaev 2020; Younas et al. 2022) to the solar wind due to a coronal hole, it is important to estimate the physical parameters such as the area and temperature structure.

As for dynamics, except for some of the studies (Shelke & Pande 1985; Obridko & Shelting 1989; Navarro-Peralta & Sanchez-Ibarra 1994; Insley et al. 1995), other studies (Wagner 1975, 1976; Timothy et al. 1975; Bohlin 1977; Hiremath & Hegde 2013; Japaridze et al. 2015) indicated rigid-body rotation rates of coronal holes. With a large number of data and an accurately estimated average longitude from the central meridian of the coronal holes, Hiremath & Hegde (2013) concluded that regardless of the area and latitudes, coronal holes rotate rigidly. Bagashvili et al. (2017) presented a statistical study of coronal hole (CH) rotation rates and their distribution over latitude and size. This study revealed a north-south asymmetry in the CH distribution, and most CHs lie in the northern hemisphere. Interestingly, similar to the results of Hiremath & Hegde (2013), the CH rotation rates are found to coincide with the solar tachocline and lower convection zone, suggesting a potential connection between CHs and the solar global magnetic field structure. Andreeva & Malaschuk (2023) investigated the rotational characteristics of a long-lived giant coronal hole, finding that its rotation rate was higher during the maximum phase of its development. This might indicate a connection to deeper solar layers via the global magnetic field configuration. Maghradze et al. (2022) studied the long-term variation in the latitudinal distribution of coronal holes and suggested that there are significant differences in the evolutionary shapes of nonpolar and polar coronal holes. Their migration route in the diagram suggests a possible connection to the solar magnetic field. On the other hand, Li & Feng (2019) analyzed 54 yr of hourly mean values of the solar wind velocity and identified a distinct relation between the velocity and rotation period. Specifically, higher-velocity solar wind exhibits faster rotation, while the rotation rate of the low-velocity solar wind decreases as the velocity increases. Additionally, the yearly rotation rate of the solar wind velocity does not align with the Schwabe cycle, but shows a significant negative correlation with the yearly sunspot numbers when leading by 3 yr. Moreover, Pinto et al. (2021) investigated the complex interactions between solar wind flows, the rotational state of the solar corona, and the origin of magnetic field deflections, such as switchbacks and bends observed by the Parker Solar Probe (PSP). By tracing solar wind flows to their source regions on the solar surface and using a global MHD model, the research identified regions with enhanced flow shear and magnetic field gradients, particularly around the boundaries between coronal holes and streamers and above pseudo-streamers as potential sources of these magnetic deflections observed by PSP.

As the coronal holes are unipolar magnetic flux tubes (Harvey & Sheeley 1979; Harvey et al. 1982), the condition of infinite conductivity of the corona leads to isorotation of the coronal hole flux tubes with the ambient plasma rotation. If the coronal holes rotate differentially, then the thermal wind balance equation (Brun et al. 2010) yields the temperature difference between the equator and the poles. On the other hand, if coronal holes rotate rigidly, there is no temperature difference between the equator and poles. Hence, in order to confirm whether coronal holes rotate rigidly or differentially, information regarding the latitudinal variation of thermal structure of the coronal holes is necessary.

The study of hydromagnetic perturbations evolving within an inhomogeneous background has received extensive attention in solar physics. The physics of MHD waves (which emanate from the coronal holes) is important not only for understanding the heating of the corona, but also for understanding the fast solar wind. Many MHD models (Davila 1985; Ofman 2005, and references therein) were developed to probe these phenomena, for which the strength and geometry of magnetic field structure of coronal hole are necessary. In the context of a two-dimensional inhomogeneous background, where the Alfvén velocity exhibits variations perpendicular to the magnetic field direction, researchers have explored two key mechanisms in detail. The first mechanism, known as phase-mixing (Heyvaerts & Priest 1983), involves the gradual bending of wavefronts due to differences in group velocity at different spatial locations. Hood et al. (1997) presented a solution to the Alfvén wave phase-mixing equations for a coronal hole model, showing that phase-mixing is a viable mechanism for heating the lower corona. The second mechanism, referred to as resonant absorption, concentrates the wave energy within a narrow layer where the wave frequency locally matches a characteristic frequency, such as the Alfvén or cusp frequency. These processes have been investigated through various approaches, including the examination of normal modes within the inhomogeneous structure (Kappraff & Tataronis 1977; Mok & Einaudi 1985; Steinolfson 1985; Davila 1987; Hollweg 1987; Califano et al. 1990, 1992). Additionally, researchers have explored the evolution of the initial disturbances in the context of these mechanisms (Lee & Roberts 1986; Malara et al. 1992, 1996). Studies have also considered the effects of density stratification and magnetic field line divergence (Ruderman et al. 1998), as well as nonlinear coupling with compressive modes (Nakariakov et al. 1997, 1998).

Extensive research has also focused on the transmission of MHD waves in magnetic fields that include null points (Landi et al. 2005). Malara (2013) explored the development of small-scale structures and discontinuities in the solar wind within the context of a complex inhomogeneous magnetic field structure in a coronal open-field region. This mechanism contributes to the generation of certain discontinuities observed in the solar wind. As emphasized in a recent review by Morton et al. (2023), previous studies (Dolla & Solomon 2008; Banerjee et al. 2009; Morton et al. 2015) have consistently shown that Alfvén waves in coronal holes exhibit minimum damping, possibly due to small density variations in the quiet Sun and even smaller variations within coronal holes, along with limited energy transfer to rotational modes, resulting in a weak phase-mixing. At this point, we accept the presence of MHD waves in various magnetic structures, including in the lower parts of coronal holes, which implies permanent wave fields. These fields, under specific conditions, undergo turbulent cascading of energy among different modes, resulting in dissipation. This dissipation acts as a source of local heat and entropy production, causing the CH plasma to deviate from thermodynamic equilibrium.

Furthermore, the nature of the wave dynamics is inherently nonlinear, encompassing turbulent cascading of wave energy and interactions among different wave harmonics and plasma particles. Due to the collision-less state of the plasma in the region where fast solar wind originates, the average mean free path of particles significantly exceeds the local Debye length. Consequently, achieving a local randomization of particle velocities, leading to Maxwellian distributions, is challenging through particle interaction processes alone. Instead, the formation of particle velocity distributions is primarily influenced by interactions with local wave turbulence or other eruptive energy sources, such as magnetic reconnections or sources of impulsive plumes (Kumar et al. 2022) of varying spatio-temporal scales. These energy sources are characterized by power-law distribution spectra, especially in the inertial range of wave turbulence, as observed in previous studies (Tu & Marsch 1995; Tu et al. 1984; Vainio et al. 2003; Shergelashvili & Fichtner 2012). Furthermore, in the wave energy injection scales, the waves are generated by sources with strongly nonequilibrium statistics, deviating from Maxwellian distribution of a CH plasma.

Biermann (1951) first proposed a continuous stream of particles originating from the Sun, inspired by the investigation of the direction of comet tails. Subsequently, Parker (1958) provided the initial theoretical framework to explain the outflow of particles from the Sun and proposed the existence of the solar wind. Since Parker's seminal work, numerous spacecraft missions and ongoing research have provided a wealth of data and insights into the complex behavior of the solar wind. For example, Bale et al. (2019) by using Parker Solar Probe data showed that low-latitude coronal holes are a key source of the slow solar wind and suggested that micro-instabilities play a major role in heating the coronal plasma. The study also reported a measured magnetic field structure that exhibited patches of large intermittent reversals (known as switchbacks) that are associated with jets of plasma and an enhanced Poynting flux. Kasper et al. (2019) studied the slow solar wind emerging from equatorial coronal holes and discovered Alfvén velocity spikes and rotational flows in the solar wind. Recently, Telloni et al. (2022) detected a switchback using the METIS coronagraph on board Solar Orbiter and reported that the switchback was generated by interchange reconnection between the coronal loops formed above an active region and the nearby open-field regions. However, neither of these observations determined whether magnetic switchbacks originate at the formation height of the 195 Å line (images of which we used for our analysis here) or above. The magnetic switchback observations were made at a height far from the height of origin of the 195 Å line ($1.1\,R_{\odot}$). It also remains unclear at which height the solar wind originates.

Although the general consensus is that the geometry of the coronal hole magnetic field structure is unipolar, to our best knowledge, no study is available to date that estimates the magnetic field strength of a coronal hole in 195 Å that probably originates in a solar radius of (Fig. 2 of Yang et al. 2009) around 1.1.

In addition to the importance of the physical parameters of a CH for the study of the solar-terrestrial relation, the following questions also have to be addressed in order to resolve the fundamental problems presented in the previous paragraphs. To summarize, (i) the variation in the physical properties, such as the area, the radiative flux, the energy and the temperature structure during the evolution passage of CH over the observed solar disk.

(ii) The dependence of these physical parameters of CH on heliographic latitude. (iii) Obtaining information about whether CH rotates rigidly or differentially from the latitudinal variation of temperature structure of CH. (iv) The strength of magnetic field structure of CH at the height of coronal region around 1.1 $R_\odot$ where the line 195 Å originates. In order to solve these problems, we used near-equatorial coronal holes for our study. Preliminary results of this study are presented in arXiv (Hiremath & Hegde 2022). More refined and final results are presented in this paper.

2. Data and estimation of different physical parameters of CH

For 2001–2008, we used 195 Å full-disk images obtained by EIT on board SOHO, although the onboard instrument also observes full-disk EUV images in other wavelength (171 Å, 284 Å, and 304 Å) passbands. A detailed description of the instrument was provided by Delaboudinière et al. (1995). The obtained images are in FITS format, and individual pixels are in units of data number (DN s^{-1}). DN is defined to be the output of the instrument electronics, which corresponds to the incident photon signal converted into charge within each CCD pixel (Madjarska & Wiegelmann 2009). Further details of SOHO/EIT 195 Å images, their calibration, the method of detection of CH with an estimation of the heliographic coordinates (e.g., latitude θ and longitude l) and, the computation of the total DN counts (TDN) of coronal holes were described in our previous study (Hiremath & Hegde 2013). In the present study, we mainly concentrate on the data of near-equatorial coronal holes that are distributed with in 40 deg north to 40 deg south. Three additional criteria used to select the data are listed below. (i) In order to minimize the projection effects (especially coronal holes near the eastern and western limbs), we only considered coronal holes that emerged within 65° of the central meridian distance. (ii) The coronal holes must be compact, independent, and not elongated in latitude. (iii) During the passage of the coronal holes across the solar disk, the hole should not merge with another coronal hole.

2.1. Computation of the area of the coronal hole

As described in our previous study (Hiremath & Hegde 2013), when the boundary of a CH is detected, the total number of pixels (TNP) within the detected boundary was estimated, and the area A of the coronal hole and its measured uncertainty δA were computed as follows:

$$A = c_1 \frac{\mathrm{TNP}}{\cos\, l} \quad \mathrm{cm}^2, \tag{1}$$

$$\delta A = c_1(\mathrm{TNP})(\tan l s\, l)\delta l \quad \mathrm{cm}^2, \tag{2}$$

where the multiplicative constant term c_1(=3.573 × 10^{16}) was estimated from the resolution of the pixel size, and the factor $1/(\cos\, l)$ (l is the viewing angle or the longitude from the central meridian) is a correction factor for the projectional effect for the CH that are close to the limb.

2.2. Computation of the average radiative flux of a coronal hole at L_1

To estimate the radiative flux F of a CH at the Lagrangian point L_1 in space, we used information from the SOHO/EIT instrumental response curve (a postscript file *calib.ps* was obtained from the website[1]). However, according to information from the SOHO/EIT website, CH data in 195 Å are also sensitive to another three wavelength (171 Å, 284 Å, and 304 Å) bands whose contributions to the instrumental responses were computed judiciously in the following way. By integrating the area under the curve, we estimated the response values of R_1, R_2, R_3, and R_4 for all four (171 Å, 195 Å, 284 Å, and 304 Å) wavelength channels. First, we manually digitized all four response curves (see Table 1), and we computed the integrated area under the curve with the trapezoidal rule method. Finally, a grand average response $R = (R_1 + R_2 + R_3 + R_4)/4$ was computed. The results of the average responses for the different channels are presented in Table 1.

Table 1. Digitized values of the instrumental response curves.

λ Å	R1	R2	R3	R4
170	2e–15	1.0e–16	1.0e–16	1.0e–16
180	1.5e–12	3e–13	7e–16	5e–15
190	5e–14	6e–12	8e–16	4e–15
200	1.5e–14	8e–13	9e–16	4e–15
210	6e–15	1.5e–13	1e–15	5e–15
220	8e–15	7e–14	1.5e–15	6e–15
230	6e–15	5e–14	1.5e–15	7e–15
240	3e–15	3e–14	2.5e–15	9e–15
250	2.5e–15	2e–14	4e–15	1.1e–14
260	1.5e–15	1.5e–14	2e–14	1.5e–14
270	1.5e–15	9e–15	1.1e–13	3e–14
280	9e–16	7e–15	3e–13	7e–14
290	6e–16	4e–15	2e–14	1.5e–13
300	4e–16	2e–15	3e–16	4e–13
310	1.5e–16	9e–16		3.8e–13
320		4e–16		9e–14
330		2e–16		9e–15
340				1.2e–15
Avg. =	4.43465e–15	1.75493e–14	1.40760e–15	2.60490e–15

Notes. The unit of the instrumental responses (R_1 to R_4) is (DN s^{-1})/(photons cm^{-2} s^{-1} steradian^{-1} $Å^{-1}$).

As the EIT instrumental response function R is in units of DN s^{-1}/(photons cm^{-2} s^{-1} steradian^{-1} $Å^{-1}$), we divided the measured TDN (total number of DN counts s^{-1} of CH) by the instrumental response function R in order to obtain the radiative flux emitted by the CH. Hence, the total radiative flux F emitted by the whole region of the CH is

$$F = c_2 \frac{\mathrm{TDN}}{R} \sin\theta \,\mathrm{photons\,cm^{-2}\,s^{-1}\,Sr^{-1}}, \tag{3}$$

and its error δF is

$$\delta F = c_2 \left[\left(\frac{\mathrm{TDN}}{R}\right)\cos\theta\delta\theta + \sin\theta\delta\left(\frac{\mathrm{TDN}}{R}\right)\right] \mathrm{photons\,cm^{-2}\,s^{-1}\,Sr^{-1}},$$

where the multiplicative constant factor $c_2 = 2.38 \times 10^{-6}$ was computed from the average of all the four wavelengths (171 Å, 195 Å, 284 Å, and 304 Å) in order to eliminate the term $Å^{-1}$ in the instrumental response curve R. Similarly, the equation of the radiative flux F1 at the Lagrangian point L1 (near Earth) is

$$F1 = c_3 \frac{\mathrm{TDN}}{R} \sin\theta \,\mathrm{photons\,cm^{-2}\,s^{-1}\,Sr^{-1}}, \tag{4}$$

[1] http://umbra.nascom.nasa.gov/eit/eit_guide/

where $c_3 = c_2 A/D^2$ (A is the area of the CH, and D is the constant distance between the Sun and the orbit of the SOHO satellite). The uncertainty on the radiative flux $\delta F1$ of CH is computed as follows:

$$\delta F1 = \left[c_3 \left(\frac{\mathrm{TDN}}{R}\right) \cos\theta \delta\theta + \left(\delta c_3 \frac{\mathrm{TDN}}{R}\right) \sin\theta + c_3 \delta \left(\frac{\mathrm{TDN}}{R}\right) \sin\theta \right] \text{photons cm}^{-2}\,\text{s}^{-1}\,\text{Sr}^{-1}, \quad (5)$$

where δc_3 is the error in c_3, and $\delta(\mathrm{TDN}/R)$ is the error in (TDN/R).

2.3. Computation of the average radiative energy emitted by the coronal hole at L_1

The total radiative energy E emitted by the CH is

$$E = h\nu F_1 \text{ ergs cm}^{-2}\,\text{s}^{-1}, \quad (6)$$

where $h\nu$ (h is Planck's constant, and ν is the radiation frequency) is a quanta of the photon energy of the EUV radiation. The uncertainty δE on the energy is

$$\delta E = h\nu \delta F_1 \text{ ergs cm}^{-2}\,\text{s}^{-1}. \quad (7)$$

2.4. Computation of the average temperature structure of the coronal hole in the corona

Spectroscopic methods yield the temperature along the observed slit, but we measured the average temperature of the observed whole coronal hole, which we call the temperature structure.

From the information of the radiative energy (I_{CHL}) of the CH at the Lagrangian point L_1, the following ratio yields the radiative energy (I_{CHS}) of the CH in the corona:

$$\frac{I_{\mathrm{CHS}}}{I_{\mathrm{CHL}}} = \frac{\int (E\cos\theta \mathrm{d}\theta) A/{R_{\mathrm{CH}}}^2}{\int (E\cos\theta \mathrm{d}\theta) A/{R_{\mathrm{CHL}}}^2} = \frac{{R_{\mathrm{CHL}}}^2}{{R_{\mathrm{CH}}}^2}, \quad (8)$$

where R_{CHL} is the distance between the solar center and the Lagrangian point L_1, and R_{CH} is the distance between the center of the Sun and the height at which the CH is formed in the corona. By knowing the values of R_{CH}, as observed, the CH in 195 Å is formed at a height of $\sim 1.1\,R_\odot$ (where $R_\odot$ is the radius of the Sun; see Fig. 2 of Yang et al. 2009), and R_{CHL}, the ratio of the right-hand side of Eq. (8), is estimated to be $\sim 3.14 \times 10^4$. Hence, we obtain $I_{\mathrm{CHS}} = 3.14 \times 10^4 I_{\mathrm{CHL}} = 3.14 \times 10^4 (\mathrm{TDN}\sin\theta)/R$. When we assume that the plasma of the CH is in thermodynamic equilibrium, the total energy radiated by the CH is equated with Planck's law, and the average temperature structure T and its uncertainty δT of the CH at the corona are computed as follows:

$$T = \frac{hc}{\lambda k \ln\left(\frac{2hc^2}{\lambda^5 I_{\mathrm{CHS}}} + 1\right)} K, \quad (9)$$

$$\delta T = \frac{2kcT^2 \frac{\delta I_{\mathrm{CHS}}}{I^2_{\mathrm{CHS}}}}{\left(\frac{2hc^2}{I_{\mathrm{CHS}}\lambda} + \lambda^4\right)} K, \quad (10)$$

where c is the velocity of light, λ is the observed wavelength, and k is the Boltzmann constant, and, I_{CHS} and δI_{CHS} are the radiative energy and its uncertainty of the CH in the corona. To justify the CH plasma in thermodynamic equilibrium, we considered a few near-equatorial coronal holes and estimated their average intensity. The coronal hole intensities are almost uniform throughout the CH, indicating that the plasma temperature is also uniform throughout the CH region. Hence, it is not surprising that previous studies (Heinemann et al. 2021) also arrived at a similar conclusion. However, very few coronal holes have an intensity enhancement near the coronal hole boundaries. Except for this limitation, we assumed the condition of thermodynamic equilibrium. Moreover, the estimated temperature of CH in each latitude zone is the average of the temperature of many coronal holes that minimize the brightening due to the CH boundaries. Considering these important facts, thermodynamic equilibrium might be a more reasonable approximation for CH images that originated at $1.1\,R_\odot$.

However, although the observed CH intensity is uniform (or at a constant temperature) parallel to the observed disk in 195 Å, significant temperature gradients are observed in the radial direction, implying that the plasma cannot be in thermodynamic equilibrium. Instead, these temperature gradients sustain the initiation and acceleration of solar wind flow patterns, suggesting a stationary nonequilibrium state. However, the assumption of local thermodynamic equilibrium serves as the zeroth-order approximation for evaluating the photon flux rates and their interpretation. Additionally, considering the origin of the fast solar wind in coronal hole flux tubes and the critical sonic point at lower heights (see, e.g., Esser et al. 2005; Tu et al. 2005) compared to the slow solar wind, the regions with 195 Å emission sources may not be entirely insensitive to both the stationary nonequilibria and transient thermal instability events (due to magnetic reconnection or impulsive plumes of different spatio-temporal scales), at least partially.

3. Results

As in our previous study (Hiremath & Hegde 2013), we followed a similar method to bin the CH data for different latitudes. A typical coronal hole in the southeastern quadrant of the SOHO/EIT image observed on 4 Jan 2001 is presented in Fig. 1a. A separated coronal hole with its boundary detected from the threshold criterion (see the details in Sect. 2 of Hiremath & Hegde 2013) is presented in Fig. 1b. We define the apparent life span τ (the actual life span is longer) as the number of observed days of the first and last appearance of the CH on the same side of the solar disk. In this way, the observed coronal holes with different life spans (a minimum of 4 days to a maximum of 10 days) that appear at different latitudes and between +65° to −65° longitude from the central meridian are illustrated in Fig. 2a. With the constraint that coronal holes that occur between +40° (northern hemisphere) to −40° (southern hemisphere) latitude zones, 113 coronal holes with different life spans ultimately yield 796 data points for our analysis. As the minimum life span of a coronal hole is 4 days, transient coronal holes (that have life span ≤2 days; Kahler & Hudson 2001) that might have different physical properties are not included in this analysis. Regardless of their life spans and after binning the coronal holes between 0–5°, 5–10°, and so on, the average latitudes of CH were computed. Figure 2b illustrates the distribution of the 796 observed data points in different latitude bins. SOHO/EIT response curves for different channels are illustrated in Fig. 3.

For the typical two coronal holes (the first CH is observed in the southern (latitude ∼30°) hemisphere, and the second CH is observed in the northern (latitude ∼13°) hemisphere) and following the methods presented in Sect. 2, the daily estimated different physical parameters are presented in Table 2. To compare the

Fig 1(a)

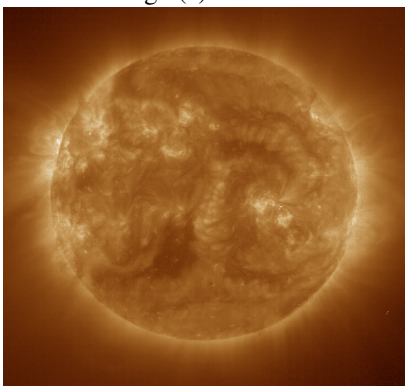

Fig 1(b)

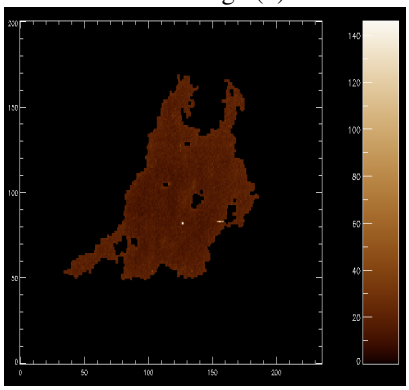

Fig. 1. (a): full-disk SOHO/EIT 195 Å image of 04-01-2001, 00:00:11 UT with detected CHs. (b): contour map of the southern CH with a given threshold.

Fig 2(a)

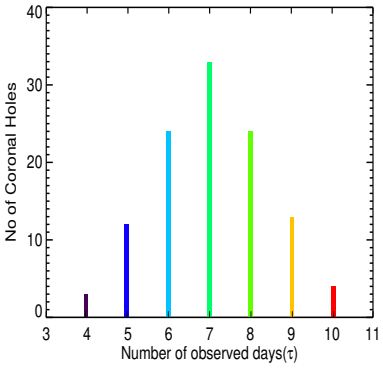

Fig 2(b)

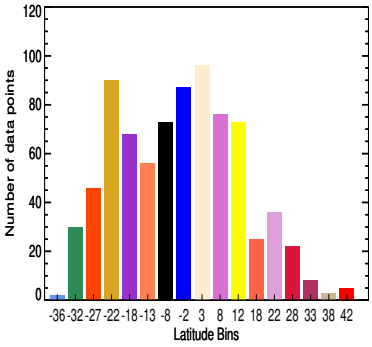

Fig. 2. (a): coronal hole count across varying lifespans on the solar disk. (b): coronal hole count across latitude bins in both hemispheres.

temperature structure of the CH computed from our method, by employing filter ratio technique, we also computed the temperature structure. For example, Hinode/XRT data on 12/02/2007 and 15/08/2007 taken with the Al-mesh/Al-poly filters are considered for the temperature measurement. We followed the filter ratio method of Narukage et al. (2011) and estimated the temperature structure of these two CHs. The temperature structure of the CH estimated with our method and the temperature structure of the CH estimated with the method of Narukage et al. (2011) is of the same order. Because the two methods yielded the same temperature structures for 113 coronal holes, we confidently computed all the physical parameters (as defined in Sect. 2).

Our first objective was to understand the daily evolution of a coronal hole during its passage across the observed solar disk. For example, regardless of their life spans and latitudes, Fig. 4 shows for the longitudes from the central meridian between +65° to −65°, which are combined in the two latitudes, the daily evolution of the area (A), the radiative flux (F) on the Sun, the radiative flux near the Earth (to be specific, at the Lagrangian point L_1 where the SOHO spacecraft is positioned) (F_1) and the temperature structure (T) of the CH on the Sun. A second-degree polynomial (quadratic) yields the best fit for the daily variation of the CH. The different estimated physical parameters (C_0, C_1, and C_2) of the polynomial fit with their respective uncertainties (δC_0, δC_1, and δC_2) and χ^2 (the measure of the goodness of fit) values are presented in Table 3.

The daily variations in the radiative flux of the CH may be useful for studies of the Earth's ionosphere (Bauer 1973; Hinteregger 1976; Roble & Schmidtke 1979; Richards et al. 1994; Lilensten et al. 2007; Dudok de Wit & Watermann 2010; Kretzschmar et al. 2009). According to Bauer (1973), one of the principal sources of ionizing radiation (the others are solar X-ray photons, galactic cosmic rays, solar cosmic-ray protons, etc.) that form planetary ionospheres is solar EUV. Although all the EUV photons from the entire solar disk can ionize planetary atmospheres, the EUV photons from coronal holes have more momentum that probably disturbs the ambient planetary ionospheres. This means that the transient behavior of EUV photons of the coronal holes probably leads to transient or sudden disturbances in the planetary ionospheres.

Thermal and magnetic field structures of the coronal holes

Knowing the thermal structure is very important to understand the fast solar wind that emanates from the coronal hole (Hegde et al. 2015, and references therein). It is also important to examine whether the thermal structure of the coronal hole is independent of or dependent on the latitude, which in turn may give a clue as to why high-latitude coronal holes have a high solar wind velocity compared to the low-latitude or equatorial coronal holes (McComas et al. 2002) during the minimum period. It is also interesting to examine if based on the thermal pressure of a coronal hole (when the CH is a magnetic flux tube, the thermal pressure in the CH is a combination of plasma and magnetic pressure) the magnitude of the average magnetic field structure of coronal holes at the corona can be measured. Important observed physical parameters such as thermal and magnetic structures are essential for probing the depth (Hiremath & Hegde 2013) and structure of the coronal holes. In the following study, we estimate the temperature structure first by estimating the radiative flux with the assumption of thermodynamic equilibrium. This temperature structure is called the total temperature. The assumption of thermodynamic equilibrium is almost the same as the assumption employed in differential

Table 2. Daily variation in the different physical parameters of coronal holes.

Area E+20	δArea E+20	FS [1] E+13	δFS [2] E+13	FAU [3] E+8	δFAU [4] E+8	ES [5] E+3	δES [6] E+3	EAU [7] E−2	δEAU [8] E−2	T [9] E+6	δT [10] E+6
1–5 Jan. 2001											
5.124	0.680	5.637	0.445	1.319	0.115	5.694	0.470	1.332	0.118	1.075	0.007
5.286	0.391	5.868	0.515	1.416	0.084	5.927	0.312	1.431	0.112	1.057	0.005
5.058	0.199	5.354	0.514	1.237	0.152	5.407	0.341	1.249	0.157	1.045	0.004
4.788	0.122	4.571	0.215	0.999	0.047	4.617	0.312	1.009	0.107	1.034	0.001
4.732	0.101	5.658	0.238	1.223	0.561	5.715	0.390	1.235	0.523	1.048	0.005
1–6 Jan. 2001											
Area E+20	δArea E+20	FS E+12	δFS E+12	FAU E+7	δFAU E+7	ES E+2	δES E+2	EAU E−3	δEAU E−3	T E+6	δT E+6
2.790	0.106	1.537	0.403	1.958	0.521	1.651	0.155	1.978	0.526	1.191	0.003
3.423	0.060	2.273	0.596	3.553	0.936	2.967	0.230	3.588	0.945	1.162	0.002
3.145	0.025	2.242	0.532	3.220	0.766	2.430	0.227	3.252	0.774	1.164	0.001
2.754	0.079	2.016	0.411	2.535	0.524	1.661	0.204	2.561	0.053	1.153	0.002
1.642	0.092	2.018	0.515	0.861	0.013	4.058	0.116	0.870	0.019	0.960	0.001
1.552	0.177	2.283	0.514	0.808	0.012	2.406	0.115	0.817	0.077	0.955	0.001

Notes. [1]Average radiative flux (photons cm^{-2} s^{-1} Sr^{-1}) of the CH measured on the Sun. [2]Uncertainty in the radiative flux of the CH measured on the Sun. [3]Average radiative flux (photons cm^{-2} s^{-1}) of the CH estimated at the Lagrangian point L_1. [4]Uncertainty in the radiative flux of the CH measured at the Lagrangian point L_1. [5]Average radiative energy (ergs cm^{-2} s^{-1} Sr^{-1}) of the CH measured on the Sun. [6]Uncertainty in the radiative energy of the CH measured on the Sun. [7]Average radiative energy (ergs cm^{-2} s^{-1}) of the CH estimated at the Lagrangian point L_1. [8]Uncertainty in the radiative energy of the CH measured at the Lagrangian point L_1. [9]Average temperature (K) of the CH measured on the Sun. [10]Uncertainty in temperature of the CH measured on the Sun.

emission measures (for example Hahn et al. 2011) to estimate the temperature structure of coronal holes. Furthermore, by using the observed density of the CH, we compute the total pressure. The obvious reason for calling total pressure is that the CH is a magnetic flux tube whose total pressure is the combination of thermal and magnetic pressures. This concept is invoked based on Parker's (Parker 1955) idea, according to which a combination of gas and magnetic pressure in the flux tube is balanced by the external gas thermal pressure when the magnetic flux tube is in hydrostatic equilibrium. In the following section, we not only derive the actual temperature structure, but also estimate the average magnetic field structure of the coronal hole using information of the estimated total temperature and pressure.

3.1. Latitudinal variation of the thermal structure of coronal holes

As described in Sect. 2, we estimated the different physical parameters of the CH that occur between +65° to −65° longitude from the central meridian. Following Hiremath & Hegde (2013), in both the hemispheres, we collected and computed for each latitude bin of 5° the average physical parameters with their respective standard deviations σ. For different latitudes, the variation in the different physical parameters such as the area, the radiative flux (on the Sun and near Earth at the Lagrange point L_1), and the total temperature structure of the CH are presented in Fig. 5. For example, the least-squares fit (of the form $Y(\theta) = C_0 + C_1 \sin^2\theta$, where θ is the latitude, C_0 and C_1 are the constants to be estimated from the least-squares fit, and Y represents different physical parameters) of area-latitude curve shows that equatorial coronal holes have a larger area than high-latitude coronal holes on average. Other illustrations of the radiative flux and temperature structures follow inverse latitudinal variations, however.

From the latitudinal variation in the total temperature and the observed density structure (Doschek et al. 1997) and so on of coronal holes, we estimated the total pressure P (=$2n_e kT$, where n_e is the number of the electron density, k is the Boltzmann constant, and T is the estimated total temperature. We assumed that the coronal hole plasma has the same number of electrons and the same proton density, hence the number 2 is multiplied). Regardless of the CH areas, in Fig. 6a, we present the variation in the total pressure CP with respect to latitude.

Many previous studies (Zhang et al. 2007; Landi 2008) concentrated on a single coronal hole and estimated the average temperature structure. Despite the variation in the thermal structure (e.g., observed David et al. 1998; Landi 2008; Landi & Cranmer 2009; Hahn et al. 2011 and theoretical Osherovich et al. 1985) inferences of the coronal hole at different heights in the corona are available, but no studies of the latitudinal variation in the thermal structure of coronal holes are available. Our results of the latitudinal variation in the thermal structure of coronal holes is the first such study.

3.2. Estimating the strength of the magnetic field structure of the coronal holes

Figure 6a shows that the total pressure of the coronal hole depends upon the latitude, such that equatorial coronal holes have lower pressure than high-latitude coronal holes. When it is accepted that a coronal hole is a magnetic flux tube, then the total pressure in the coronal hole is the sum of the plasma and magnetic pressure. The best analogy (except for strong magnetic fields in sunspots) for magnetic flux tubes (sunspots) and a coronal hole can be obtained from previous (Fla et al. 1984; Davila 1985; Osherovich et al. 1985; Obridko & Solov'ev 2011; Terradas et al. 2022; Ofman 2005, and references therein) MHD models.

Hence, when we accept that the plasma pressure of coronal hole is independent of the latitude, then one possible interpretation of the latitudinal variation in the total pressure of the coronal

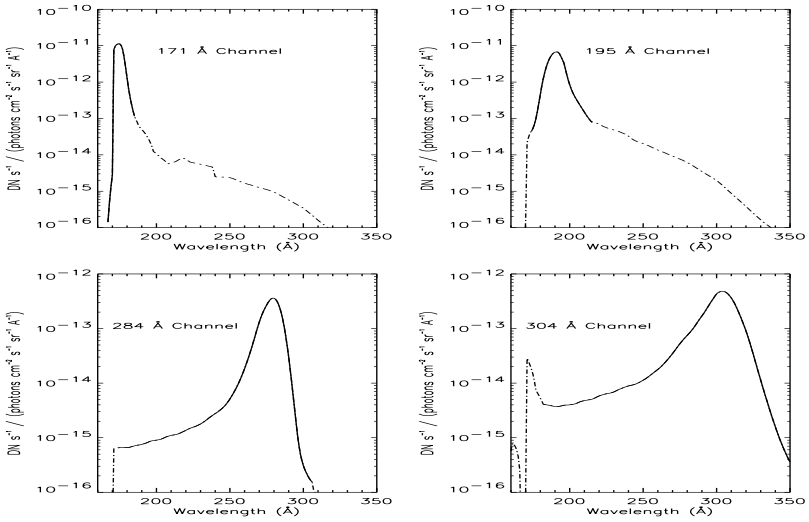

Fig. 3. SOHO/EIT Response Curves for various observed channels (171 Å, 195 Å, 284 Å and 304 Å). Image credit: http://umbra.nascom.nasa.gov/eit/eit_guide/

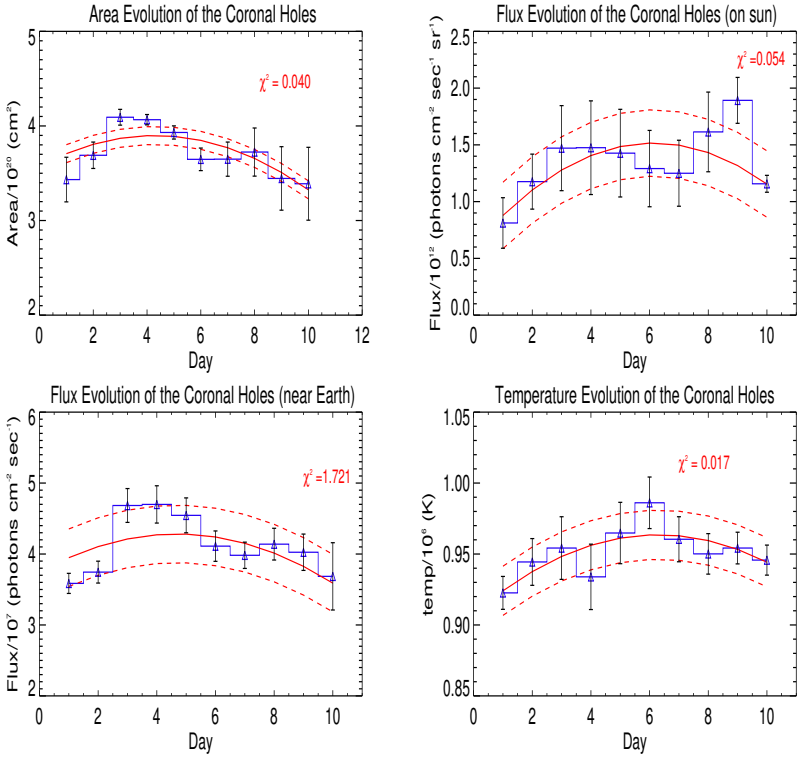

Fig. 4. Daily variation of estimated coronal hole physical parameters (shown as blue triangles). The continuous red line represents a least-squares fit and dashed red lines depict one standard deviation error bands computed from all data points. χ^2 measures goodness of fit.

Table 3. Estimated CH parameters.

Parameters	C_0	δC_0	C_1	δC_1	C_2	δC_2	χ^2
$A \times 10^{20}$	3.57	0.83	0.15	0.30	−0.02	0.02	0.040
$F \times 10^{11}$	6.06	0.30	2.97	0.70	−0.20	0.06	0.054
$F1 \times 10^{7}$	3.70	0.90	0.23	0.10	−0.03	0.01	1.721
$T \times 10^{6}$	0.91	0.30	0.02	0.04	−0.001	0.004	0.017

holes could be that it is caused by the contribution from the magnetic pressure. This means that when the latitudinal variation in the magnetic field structure of coronal holes is known, the magnetic pressure can be computed and can be subtracted from the estimated total pressure. Unfortunately, to our best knowledge, there are no studies that give information about the latitudinal variation in the magnetic field structure of coronal holes in the corona. We therefore adopted the following method to compute the magnetic field structure and hence the magnetic pressure of a coronal hole in the corona.

First, we made the reasonable assumption that a coronal hole is a magnetic flux tube that is probably anchored below

Table 4. Estimated CH parameters.

Parameters	C_0	δC_0	C_1	δC_1	χ^2
$A \times 10^{20}$	3.80	0.50	−0.50	0.10	1.409
$F \times 10^{12}$	1.30	0.08	0.50	0.20	6.986
$F1 \times 10^{7}$	4.40	0.30	0.70	0.50	0.405
CT $\times 10^{6}$	0.93	0.40	0.17	0.14	0.041
CP $\times 10^{-2}$	0.97	0.20	0.17	0.15	0.041
Photospheric $\|B\|$	6.25	0.59	11.89	2.44	0.718
Corona $\|B_c\|$	0.011	0.001	0.021	0.004	0.718
MP $\times 10^{-6}$	8.98	0.61	7.98	3.56	12.54
TP $\times 10^{-2}$	0.174	0.001	0.012	0.001	0.037
True temperature $\times 10^{6}$	0.9019	0.0001	0.0608	0.0007	0.037

the photosphere (Gilman 1977; Golub et al. 1981; Jones 2005; Hiremath & Hegde 2013). As the magnetic flux tube is embedded in the solar atmosphere, an increase with height from the photosphere to the corona results in a decrease in the surrounding ambient plasma pressure, and hence, the tube must expand. In the following, this statement is further corroborated by Hegde et al. (2014). Based on SDO data, for a coronal hole observed in three wavelengths, 174 Å, 193 Å, and 211 Å, the average area of a coronal hole is 0.5×10^{20} cm^2 for 174 Å, 0.98×10^{20} cm^2 for 193 Å, and 1.06×10^{20} cm^2 for 211 Å. Simultaneously, the DN counts (radiative intensity) also reduce from 174 Å, 193 Å and 211 Å. The successive increase in the line formation (Yang et al. 2009) for 174 Å, 193 Å, and 211 Å at different heights is 1.01 $R_\odot$, 1.05 $R_\odot$, and 1.3 $R_\odot$. Within 30% of the solar radius from the photosphere, the coronal hole area increases to twice the area of the coronal hole in the photosphere. It is therefore reasonable to consider that the coronal hole expands from the photosphere to the corona, where the 195 Å line originates.

Furthermore, when we accept that a coronal hole is a Parker flux tube (Parker 1955), then the magnitude of the magnetic field structure B inside the coronal hole is directly proportional to ${P_e}^{1/2}$ (where P_e is the external ambient pressure of the plasma). Hence, with this simple relation, we can estimate the strength of the magnetic field structure B_c of the coronal hole at the corona when we know the strength of the magnetic field structure and the ambient plasma pressures at different heights. To be specific, the resulting derivation is (i.e., obtained from the above simple relation) $B_c = B_{pho}\ (P_{ce}/P_{pho})^{1/2}$ (where B_c and P_{ce} are the strength of the magnetic field structure of the coronal hole and the ambient plasma pressure in the corona, and B_{pho} and P_{pho} are the strength of the magnetic field structure of the coronal hole and the ambient plasma pressure in the photosphere). For the strength of the magnetic field structure B_{pho} of the coronal hole in the photosphere, we considered the unsigned inferred strength of the magnetic field $|B|$ of the CH in the photosphere that was obtained by analyzing HMI data (Heinemann et al. 2019). This inferred field from the photospheric magnetograms is the line-of-sight component. With the above formula and using the ambient external pressure in the photosphere and the corona (Aschwanden 2004), we estimated the magnetic field structure B_c (and hence, the magnetic pressure $B_c^2/4\pi$) of the coronal hole in the corona (around 1.1 $R_\odot$, where the 195 Å line originates).

After binning in different latitude zones, the latitudinal variation in the average strength of the unsigned magnetic field structure $|B|$ of the coronal hole in the photosphere is presented in Fig. 6b. As we reasoned above, the magnitude of the magnetic field structure (and the magnetic pressure) of the coronal hole in the photosphere indeed increases from the equator to higher latitudes. If coronal holes are magnetic flux tubes, the conservation of the magnetic flux should yield the inverse relation of the area-latitude relation. Hence, it is not surprising that in Fig. 5a, coronal holes close to the equator have larger areas than coronal holes near higher latitudes.

The estimated strength of the magnetic field structure $|B_c|$ of the coronal hole and its magnetic pressure (MP) in the corona are presented in Figs. 6c and d, respectively. The magnitude of the magnetic field structure of a coronal hole in the corona is estimated to be ∼0.01(±0.001) Gauss on average.

The estimated strength of the magnetic field might be different from the actual strength of the magnetic field structure for the following two reasons. First, the observed magnetic field structure of the coronal hole estimated from the photospheric magnetogram is longitudinal, and hence, the inferred magnetic field of the coronal hole in the corona is also a longitudinal component. For the radial component of the magnetic field (a field structure like this is invoked to model the coronal hole), however, the strength of the longitudinal component of the magnetic field of the coronal hole appears to be underestimated because the radial field is $B_l/\cos(\lambda - \phi)$ (where B_l is the longitudinal component of the magnetic field, λ is the latitude, which varies from 0 to 90 deg from the equator to the pole, and ϕ is the inclination angle of the rotational axis of the Sun). Second, and according to Parker's (Parker 1955) flux tube model, the estimated strength of the magnetic field depends upon the square root of the ambient pressure, which ultimately is model dependent. Hence, it cannot be ruled out that some uncertainty (0.001 ∼ 10%) persists, which is reflected in the estimated strength of the longitudinal component of the magnetic field from the least-squares fit. However, we know of no study that estimated strength of the magnetic field of the coronal hole observed in 195 Å.

By knowing the latitudinal variation in the strength of the magnetic field structure $|B_c|$ of the coronal hole, the estimated magnetic pressure was subtracted from the total pressure of the coronal hole, and the actual thermal pressure of the coronal hole was computed (Fig. 7a). By knowing the electron density and thermal pressure, the actual temperature structure of coronal hole is computed, and its latitudinal variation is presented in Fig. 7b. Averaged over all latitude regions, the mean temperature of the coronal hole is estimated to be ∼0.94 K. This magnitude is the same as the magnitude obtained from previous studies (Saqri et al. 2020; Heinemann et al. 2021). From these figures, we find that the variation in the temperature structure of the

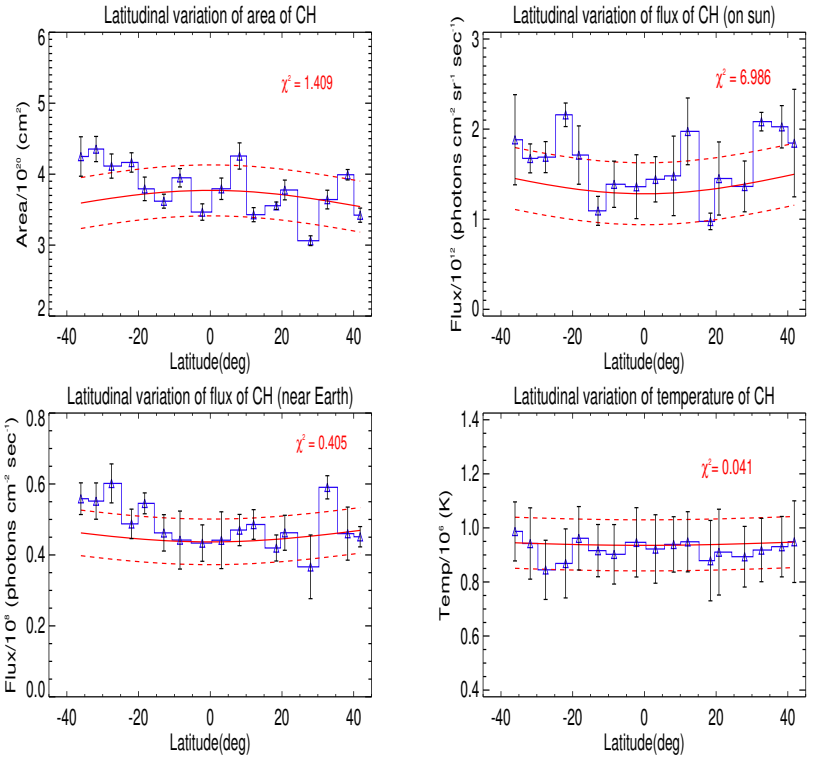

Fig. 5. Variation of coronal hole physical parameters across latitudes. Figure illustrates the variation of different physical parameters (shown as blue triangles) such as the area, radiative flux emitted by the coronal hole on the Sun and at the Lagrangian point L_1, and the apparent temperature structure of the coronal hole across latitudes. The continuous red line represents a least-squares fit and dashed red lines denote one standard deviation error bands, computed from all data points. While χ^2 serves as a measure of the goodness of fit.

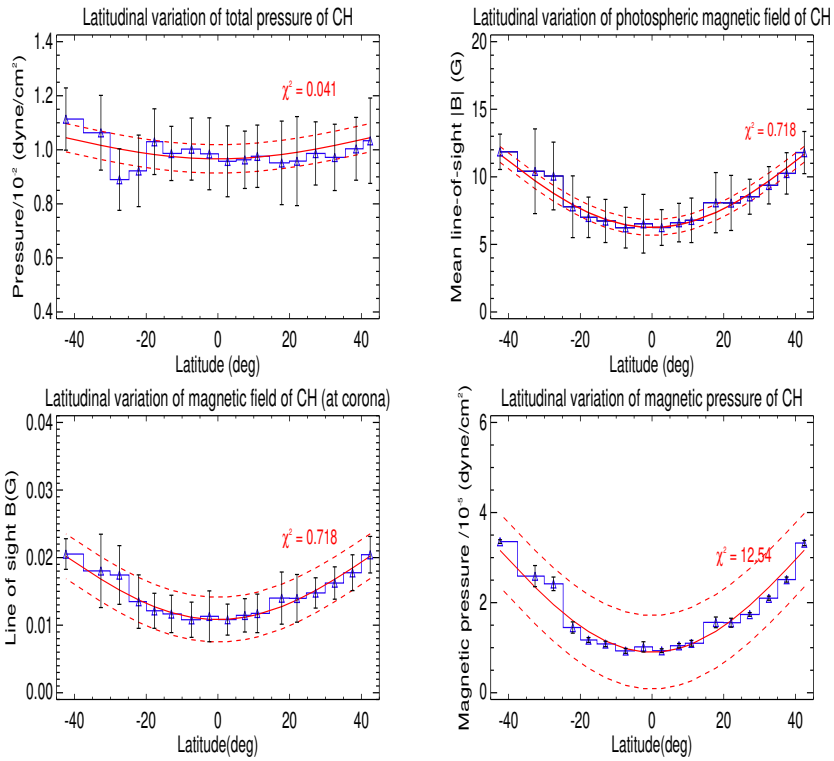

Fig. 6. Variation of coronal hole physical parameters across latitudes. Figure illustrates the variation of different physical parameters (depicted as blue triangles) such as total pressure, magnitude of magnetic field structures in the photosphere and corona, and magnetic pressure of the coronal hole across latitudes. The continuous red line represents a least-squares fit and dashed red lines depict one standard deviation error bands computed from all data points. While χ^2 serves as a measure of the goodness of fit.

coronal holes is independent of the solar latitude. This important result also agrees with a previous study (Gopasyuk et al. 2020), which reported that the temperature of the equatorial coronal holes is similar to that of polar coronal holes.

To estimate the CH temperature, the results presented in Figs. 6d and 7a are useful to verify the assumption of thermodynamic equilibrium in the following way. If there is a strong magnetic field structure, then the temperature structures along and perpendicular to the magnetic field are different. However, the estimate from our analysis yields an average magnetic pressure of the CH that is very low ($\sim 10^{-5}$ dyne cm^{-2}) compared with the strong plasma pressure ($\sim 10^{-2}$ dyne cm^{-2}) at the height of the observed 195 Å line. Hence, the plasma pressure and energy (or the inferred temperature) of the CH appear to be spatially uniform. Thus, an assumption of CH plasma in thermodynamic equilibrium at this height is a good approximation. One more

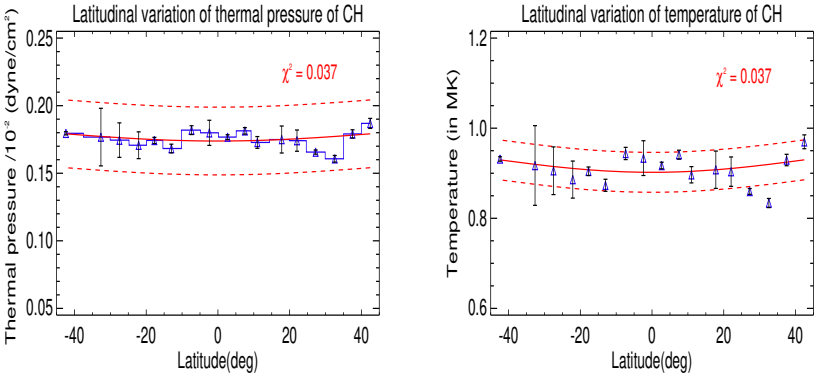

Fig. 7. Corona hole thermal pressure and temperature variation (shown as blue triangles) across latitudes. The continuous red line represents a least-squares fit and dashed red lines depict one standard deviation error bands computed from all data points. While χ^2 serves as a measure of the goodness of fit.

point to note here is that we deprojected the observed parameters using the cosine of the visible longitude. This procedure is precise when the object is transiting near the visible equator or is on the central meridian. However, this deprojection effect may not completely remove projection effects in other cases, especially very close to the limb and in the regions of higher-latitude. Hence, we emphasize that our conclusions are based on average values (Figs. 4–7) of the observed parameters.

The latitudinal variation in the different physical parameters of the CH was subjected to a least-squares fit (of the the form $Y(\theta) = C_0 + C_1 \sin^2\theta$), and the estimated coefficients C_0 and C_1 with their respective uncertainties (δC_0 and δC_1) and χ^2 values are presented in Table 4. In this table, the units are in cgs. The first column lists the area (A), the radiative flux (F) on the Sun, the flux ($F1$) near Earth, the total temperature (CT), the total pressure (CP), the strength of the coronal hole magnetic field structure in the photosphere ($|B|$) and the corona ($|B_c|$), the magnetic pressure (MP) of the coronal hole in the corona, the actual pressure (TP), and the actual (true) temperature of the coronal hole in the corona. Columns 2–5 list the coefficients and their uncertainties as estimated with the least-squares fit. The last column in Tables 3 and 4 lists the value of the χ^2 (the measure of the goodness of fit).

4. Discussion and conclusions

We discuss our two main results below. The first result is the magnitude of the magnetic field structure of the coronal holes, which increases from the equator to the two solar poles. Previous studies (Harvey et al. 1982; Webb & Davis 1985; Abramenko et al. 2009) have argued that this result could be due to the occurrence of coronal holes during the evolution of solar cycle because the polar coronal holes have stronger magnetic fields than the coronal holes at low latitudes. Although the inferred result of the latitudinal variation in the strength of the magnetic field structure of the coronal holes from our study is consistent with the results of previous studies, the question remains why high-latitude coronal holes occur with higher average magnetic field strengths than low-latitude coronal holes.

This important observed and inferred information of the latitudinal variation in the strength of the magnetic field probably suggests that the coronal hole origin is not understood consistently. Because coronal holes are unipolar magnetic field structures, their origin can be understood from the global nature of the magnetic field structure of the Sun. The following conjecture about the genesis of coronal holes is probably consistent with the result of the latitudinal dependence of the magnitude of the magnetic field structure of the coronal holes.

4.1. Genesis of coronal holes

During the period of minimum solar activity, white-light pictures taken during a total solar eclipse show a dipole-like magnetic field structure that delineates the intensity patterns (rays) that originate from the two poles. Neither observational (Stenflo 1994) nor theoretical studies (Hiremath & Gokhale 1995, and references therein) can rule out that such a large-scale global dipole-like magnetic field structure is of primordial origin. We have to make a clear distinction between the steady and time-dependent parts of the solar magnetic field structure. The steady part of the solar magnetic field structure has a timescale of billions of years (Hiremath & Gokhale 1995, and references therein). The time-dependent part of the solar magnetic field structure, on the other hand, has a 22 yr timescale. To understand the genesis of a coronal hole, in the following conjecture, we invoke the large-scale steady part of the magnetic field structure in order to be compatible with the inferred latitudinal variation in the magnetic field structure of the coronal hole.

Based on the observational (Stenflo 1994) estimate of the structure of the poloidal part of the magnetic field structure, the intensity is ~1 G. To match the 22-yr magnetic periodicity, our previous study (Hiremath & Gokhale 1995, and references therein) estimated the global solar dipole-like magnetic field structure to be ~0.01 G. This result is also consistent with the recently estimated average magnetic field structure of a CH of ~0.028 G (Kotov 2015). Although the genesis of the coronal holes is debatable, for the consistency of the inferred coronal hole magnetic field structure whose intensity increases from the equator to the pole, we present the probable mechanism of the CH formation as follows.

If the large-scale steady part of poloidal magnetic field structure is perturbed, Alfvén waves are produced, whose interference pattern leads to the formation of the coronal hole structure. If B_p is the intensity of the large-scale steady part of the magnetic field structure, then the resulting amplitude δB_p of Alfvén waves is on the same order as that of the intensity of the original magnetic field structure. That is, δB_p is $\sim B_p$. Although the steady part of the poloidal part of the magnetic field structure probably consists of a combined (uniform, dipole, and quadrupole) filed structure (Hiremath & Gokhale 1995), for the sake of simplicity, we considered a dipole-like field structure only. For a particular radius, the intensity or magnitude of the magnetic field structure varies as $\sin^2\lambda$ (where λ is the, observed latitude; here $\lambda = 0°$ is the equator and $\lambda = 90°$ is the pole), whose magnitude increases from the equator to the pole. This means, as presented in Fig. 6c, that the coronal holes that originated at the equator must have a lower magnitude of the magnetic field structure than the coronal holes that originated near the poles. When we accept the naive

concept that coronal holes are formed due to Alfvén wave perturbations of the poloidal component of the magnetic field structure, as the amplitude of magnetic field structure of the Alfvén waves is at least on the same order as that of the steady part of the magnetic field structure, it is not surprising that the average (see the fits) strength of the magnetic field structure is the same as the strength (in the range of 0.01−1 G) of the steady part of the magnetic field structure as estimated by observational (Stenflo 1994; Kotov 2015) and theoretical (Hiremath & Gokhale 1995) studies. This speculative explanation of the origin of coronal holes has to be treated with caution unless some other studies also agree with our conjecture that coronal holes originate from the Alfvén wave perturbations of the global large-scale weak magnetic field structure.

4.2. Possible explanation of the coronal hole temperature structure independent of latitude

Another interesting result is that the variation in the thermal structure (especially the actual to true temperature) of the coronal holes is independent of the latitudes. Because a coronal hole is a magnetic flux tube, for the steady state of the magnetic field structure and without gain of magnetic flux during the coronal hole evolution, the condition of infinite conductivity leads to isorotation of the coronal holes with the surrounding ambient plasma rotation. This means that the coronal hole magnetic flux bundle follows the path of isorotational contours. To be precise, coronal holes that might have formed due to Alfvén wave perturbations travel along the large-scale magnetic field structure parallel to the isorotational contours. In our previous study (Hiremath & Gokhale 1995), we showed that the steady part of the large-scale magnetic field structure may be of primordial origin and consists of the combined magnetic field structure in the radiative core and current-free (combination of dipole- and quadrupole-like field structures that are embedded in the uniform) field structure in the convective envelope, and both structures in turn isorotate with the internal solar plasma rotation, as inferred from helioseismology.

From the above discussion, it is clear that the rotation rate of the coronal holes and the rotation rate of the ambient solar plasma depend upon each other. Helioseismic inferences (Hiremath 2013, 2016, and references therein) yield a rigid-body rotation in the radiative core and differential rotation in the convective envelope. This means that if the coronal holes only originate in the convective envelope, they must rotate differentially. Otherwise, coronal holes are likely to rotate rigidly if the coronal holes originate in the radiative core. Based on theoretical (Gilman 1977; Golub et al. 1981; Jones 2005) and observational (Hiremath & Hegde 2013) inferences, it was argued that coronal holes probably originate below the convective envelope, which in turn implies that coronal holes rotate rigidly (because the radiative core rotates rigidly).

When we consider the curl of the momentum equation in the cylindrical coordinates and for a steady angular velocity gradient, the angular velocity of solar plasma is balanced (Chandrasekhar 1956; Brun et al. 2010, and references therein) by the combined forces due to the stretching or tilting of the vorticity due to the the velocity gradients, advection of vorticity by the flows, turbulent and Reynold stresses, Maxwell stresses, baroclinic forces, and so on. When we assume that other forces are negligible, then the gradient of the angular velocity is balanced by the baroclinic forces alone. In cylindrical coordinates, the relation can be expressed in the form of the equation $\frac{\partial \Omega}{\partial z} = \frac{g}{r c_p} \frac{\partial \langle S' \rangle}{\partial z}$, where Ω is the angular velocity of the solar plasma, g is the acceleration due to gravity, c_p is the specific heat at constant pressure, g/c_p is the adiabatic temperature gradient, r is the radial variation, and $\langle S' \rangle$ is the entropy of the ambient medium. This equation is called thermal wind balance equation (Brun et al. 2010). This means that unless there is a temperature difference between the pole and equator, the angular velocity of the solar plasma cannot be differential with respect to latitude and cannot be maintained either, unless the angular velocity is balanced by the toroidal magnetic field structure. As the coronal holes isorotate with the solar plasma, this equation also implies that unless there is a temperature structure that substantially varies from the equator to the pole, coronal holes cannot rotate rigidly. However, our study yields a temperature structure (and hence entropy) of coronal holes that is independent of solar latitude. Hence, the above thermal wind balance equation implies that $\frac{\partial \Omega}{\partial z} = 0$. This means that coronal holes must rotate rigidly or that the rotation rate of the coronal holes is independent of solar latitude. This reasoning also matches the results (Hiremath & Hegde 2013) of rigid-body rotation rates of coronal holes derived from SOHO 195 Å data.

To conclude this study, for 2001–2008, we used near-equatorial coronal holes detected in SOHO/EIT images to understand the area time evolution and the latitudinal variation in the thermal and magnetic field structure. The different estimated physical parameters of the coronal holes are the area $\sim 3.8(\pm 0.5) \times 10^{20}$ cm^2, the radiative flux at the Sun $\sim 2.3(\pm 0.2) \times 10^{13}$ photons cm^{-2} s^{-1}, the radiative energy $\sim 2.32(\pm 0.5) \times 10^3$ ergs cm^{-2} s^{-1}, the temperature structure $\sim 0.94(\pm 0.1) \times 10^6$ K, and the magnitude of the magnetic field structure, which we estimate to be $\sim 0.01 \pm 0.001$ G.

Acknowledgements. We are grateful to the anonymous referee for the useful comments that improved the manuscript substantially. This work has been carried out under "CAWSES India Phase-II program of Theme 1" sponsored by Indian Space Research Organization (ISRO), Government of India. SOHO is a mission of international cooperation between ESA and NASA. Hegde acknowledges Indian Institute of Astrophysics for the research support. *Contributions*: Both the authors conceived the work, analyzed the data, derived the equations. Both the authors contributed in writing Sects. 1–3. While Hiremath contributed in writing discussion (Sect. 4) part of the manuscript.

References

Abramenko, V., Yurchyshyn, V., & Watanabe, H. 2009, Sol. Phys., 260, 43
Andreeva, O. A., & Malaschuk, V. M. 2023, Geomagn. Aeron., 63, 449
Aschwanden, M. J. 2004, Physics of Solar Corona (Berlin: Springer-Verlag)
Bagashvili, S. R., Shergelashvili, B. M., Japaridze, D. R., et al. 2017, A&A, 603, A134
Bale, S. D., Badman, S. T., Bonnell, J. W., et al. 2019, Nature, 576, 237
Banerjee, D., Pérez-Suárez, D., & Doyle, J. G. 2009, A&A, 501, L15
Bauer, S. J. 1973, Physics of Planetary Ionospheres (Berlin: Springer-Verlag), 6
Biermann, L. 1951, ZAp, 29, 274
Bohlin, J. D. 1977, Sol. Phys., 51, 377
Borisenko, A., & Bogachev, S. 2023, Sol. Terr. Phys., 9, 112
Brun, A. S., Antia, H. M., & Chitre, S. M. 2010, A&A, 510, A33
Califano, F., Chiuderi, C., & Einaudi, G. 1990, ApJ, 365, 757
Califano, F., Chiuderi, C., & Einaudi, G. 1992, ApJ, 390, 560
Chandrasekhar, S. 1956, ApJ, 124, 232
Chiuderi Drago, F., Avignon, Y., & Thomas, R. J. 1977, Sol. Phys., 51, 143
Chiuderi Drago, F., Landi, E., Fludra, A., & Kerdraon, A. 1999, A&A, 348, 261
Choi, Y., Moon, Y. J., Choi, S., et al. 2009, Sol. Phys., 254, 311
Cranmer, S. R. 2009, Liv. Rev. Sol. Phys., 6, 3
David, C., Gabriel, A. H., Bely-Dubau, F., et al. 1998, A&A, 336, L90
Davila, J. M. 1985, ApJ, 291, 328
Davila, J. M. 1987, ApJ, 317, 514
Delaboudinière, J. P., Artzner, G. E., Brunaud, J., et al. 1995, Sol. Phys., 162, 291
Dolla, L., & Solomon, J. 2008, A&A, 483, 271

Doschek, G. A., & Feldman, U. 1977, ApJ, 212, L143
Doschek, G. A., & Laming, J. M. 2000, ApJ, 539, L71
Doschek, G. A., Warren, H. P., Laming, J. M., et al. 1997, ApJ, 482, L109
Doyle, J. G., Chapman, S., Bryans, P., et al. 2010, Res. Astron. Astrophys., 10, 91
Dudok de Wit, T., & Watermann, J. 2010, C. R. Geosci., 342, 259
Dwivedi, B. N., & Mohan, A. 1995, Sol. Phys., 156, 197
Dwivedi, B., Mohan, A., & Wilhelm, K. 2000, Adv. Space Res., 25, 1751
Esser, R., Fineschi, S., Dobrzycka, D., et al. 1999, ApJ, 510, L63
Esser, R., Lie-Svendsen, Ø., Janse, Å. M., & Killie, M. A. 2005, ApJ, 629, L61
Fathy, I., Amory-Mazaudier, C., Fathy, A., et al. 2014, J. Geophys. Res.: Space Phys., 119, 4120
Fla, T., Habbal, S. R., Holzer, T. E., & Leer, E. 1984, ApJ, 280, 382
Gilman, P. A. 1977, in Coronal Holes and High Speed Wind Streams, ed. J. B. Zirker (Boulder: Associated Univ. Press), 331
Golub, L., Rosner, R., Vaiana, G. S., & Weiss, N. O. 1981, ApJ, 243, 309
Gopasyuk, O. S., Baranovskii, E. A., Tarashchuk, V. P., & Shtertser, N. I. 2020, Astrophysics, 63, 421
Goyal, S. K., Kumar, P., Janardhan, P., et al. 2018, Planet. Space Sci., 163, 42
Gulyaeva, T. L., & Gulyaev, R. A. 2020, J. Atmos. Sol. Terr. Phys., 208, 105380
Habbal, S. R. 1996, Int. Astron. Union Colloq., 154, 49
Habbal, S. R., Esser, R., & Arndt, M. B. 1993, ApJ, 413, 435
Hahn, M., Landi, E., & Savin, D. W. 2011, ApJ, 736, 101
Hara, H., Tsuneta, S., Acton, L. W., et al. 1994, PASJ, 46, 493
Hara, H., Tsuneta, S., Acton, L. W., et al. 1996, Adv. Space Res., 17, 231
Harvey, J. W., & Sheeley, N. R. 1979, Space Sci. Rev., 23, 139
Harvey, K. L., Sheeley, N. R., & Harvey, J. W. 1982, Sol. Phys., 79, 149
Hegde, M., Hiremath, K. M., & Doddamani, V. H. 2014, Adv. Space Res., 54, 272
Hegde, M., Hiremath, K. M., Doddamani, V. H., & Gurumath, S. R. 2015, JApA, 36, 355
Heinemann, S. G., Temmer, M., Heinemann, N., et al. 2019, Sol. Phys., 294, 144
Heinemann, S. G., Saqri, J., Veronig, A. M., Hofmeister, S. J., & Temmer, M. 2021, Sol. Phys., 296, 18
Heyvaerts, J., & Priest, E. R. 1983, A&A, 117, 220
Hinteregger, H. E. 1976, J. Atmos. Terr. Phys., 38, 791
Hiremath, K. M. 2009, Sun Geosph., 4, 16
Hiremath, K. M. 2013, in New Trends in Atomic and Molecular Physics, ed. M. Mohan (Berlin: Springer-Verlag) 317
Hiremath, K. M. 2016, in Lecture Notes in Physics, eds. J. P. Rozelot, & C. Neiner (Berlin: Springer-Verlag), 914, 69
Hiremath, K. M., & Gokhale, M. H. 1995, ApJ, 448, 437
Hiremath, K. M., & Hegde, M. 2013, ApJ, 763, 137
Hiremath, K. M., & Hegde, M. 2022, arXiv e-prints [arXiv:2204.04410]
Hiremath, K. M., & Mandi, P. I. 2004, New Astron., 9, 651
Hiremath, K. M., Manjunath, H., & Soon, W. 2015, New Astron., 35, 8
Hollweg, J. V. 1987, ApJ, 312, 880
Hood, A. W., Gonzalez-Delgado, D., & Ireland, J. 1997, A&A, 324, 11
Insley, J. E., Moore, V., & Harrison, R. A. 1995, Sol. Phys., 160, 1
Japaridze, D. R., Bagashvili, S. R., Shergelasvili, B. M., & Chargeishvili, B. B. 2015, Astrophysics, 58, 575
Jones, H. P. 2005, in Large-scale Structures and their Role in Solar Activity, eds. K. Sankarasubramanian, M. Penn, & A. Pevtsov, ASP Conf. Ser., 346, 229
Kahler, S. W., & Hudson, H. S. 2001, J. Geophys. Res., 106, 29239
Kappraff, J. M., & Tataronis, J. A. 1977, J. Plasma Phys., 18, 209
Karachik, N. V., & Pevtsov, A. A. 2011, ApJ, 735, 47
Kasper, J. C., Bale, S. D., Belcher, J. W., et al. 2019, Nature, 576, 228
Kotov, V. A. 2015, Adv. Space Res., 55, 979
Kretzschmar, M., Dudok de Wit, T., Lilensten, J., et al. 2009, Acta Geophys., 57, 42
Krieger, A. S., Timothy, A. F., & Roelof, E. C. 1973, Sol. Phys., 29, 505
Krista, L. D., Gallagher, P. T., & Bloomfield, D. S. 2011, ApJ, 731, L26
Kumar, P., Karpen, J. T., Uritsky, V. M., et al. 2022, ApJ, 933, 21
Landi, E. 2008, ApJ, 685, 1270
Landi, E., & Cranmer, S. R. 2009, ApJ, 691, 794
Landi, S., Velli, M., & Einaudi, G. 2005, ApJ, 624, 392
Lee, M. A., & Roberts, B. 1986, ApJ, 301, 430
Lei, J., Thayer, J. P., Forbes, J. M., Sutton, E. K., & Nerem, R. S. 2008, Geophys. Res. Lett., 35, L10109
Li, K. J., & Feng, W. 2019, MNRAS, 489, 3427
Lilensten, J., Dudok de Wit, T., Amblard, P.-O., et al. 2007, Ann. Geophys., 25, 1299
Machiya, H., & Akasofu, S. I. 2014, J. Atmos. Sol. Terr. Phys., 113, 44
Madjarska, M. S., & Wiegelmann, T. 2009, A&A, 503, 991
Maghradze, D. A., Chargeishvili, B. B., Japaridze, D. R., Oghrapishvili, N. B., & Chargeishvili, K. B. 2022, MNRAS, 511, 5217
Malara, F. 2013, A&A, 549, A54
Malara, F., Veltri, P., Chiuderi, C., & Einaudi, G. 1992, ApJ, 396, 297
Malara, F., Primavera, L., & Veltri, P. 1996, ApJ, 459, 347
Marsch, E., Tu, C. Y., & Wilhelm, K. 2000, A&A, 359, 381
McComas, D. J., Elliott, H. A., & von Steiger, R. 2002, Geophys. Res. Lett., 29, 1314
Mogilevsky, E. I., Obridko, V. N., & Shilova, N. S. 1997, Sol. Phys., 176, 107
Mok, Y., & Einaudi, G. 1985, J. Plasma Phys., 33, 199
Morton, R. J., Tomczyk, S., & Pinto, R. 2015, Nat. Commun., 6, 7813
Morton, R. J., Sharma, R., Tajfirouze, E., & Miriyala, H. 2023, Rev. Mod. Plasma Phys., 7, 17
Moses, D., Clette, F., Delaboudinière, J. P., et al. 1997, Sol. Phys., 175, 571
Nakariakov, V. M., Roberts, B., & Murawski, K. 1997, Sol. Phys., 175, 93
Nakariakov, V. M., Roberts, B., & Murawski, K. 1998, A&A, 332, 795
Narukage, N., Sakao, T., Kano, R., et al. 2011, Sol. Phys., 269, 169
Navarro-Peralta, P., & Sanchez-Ibarra, A. 1994, Sol. Phys., 153, 169
Neupert, W. M., & Pizzo, V. 1974, J. Geophys. Res., 79, 3701
Nisticò, G., Patsourakos, S., Bothmer, V., & Zimbardo, G. 2011, Adv. Space Res., 48, 1490
Nolte, J. T., Krieger, A. S., Timothy, A. F., et al. 1976, Sol. Phys., 46, 303
Obridko, V. N., & Shelting, B. D. 1989, Sol. Phys., 124, 73
Obridko, V. N., & Solov'ev, A. A. 2011, Astron. Rep., 55, 1144
Ofman, L. 2005, Space Sci. Rev., 120, 67
Osherovich, V. A., Gliner, E. B., Tzur, I., & Kuhn, M. L. 1985, Sol. Phys., 97, 251
Parker, E. N. 1955, ApJ, 121, 491
Parker, E. N. 1958, ApJ, 128, 664
Peter, H., & Judge, P. G. 1999, ApJ, 522, 1148
Pinto, R. F., Poirier, N., Rouillard, A. P., et al. 2021, A&A, 653, A92
Richards, P. G., Fennelly, J. A., & Torr, D. G. 1994, J. Geophys. Res., 99, 8981
Roble, R. G., & Schmidtke, G. 1979, J. Atmos. Terr. Phys., 41, 153
Rotter, T., Veronig, A. M., Temmer, M., & Vršnak, B. 2012, Sol. Phys., 281, 793
Ruderman, M. S., Nakariakov, V. M., & Roberts, B. 1998, A&A, 338, 1118
Saqri, J., Veronig, A. M., Heinemann, S. G., et al. 2020, Sol. Phys., 295, 6
Shelke, R. N., & Pande, M. C. 1985, Sol. Phys., 95, 193
Shergelashvili, B. M., & Fichtner, H. 2012, ApJ, 752, 142
Shugai, Y. S., Veselovsky, I. S., & Trichtchenko, L. D. 2009, Geomagn. Aeron., 49, 415
Sojka, J. J., McPherron, R. L., van Eyken, A. P., et al. 2009, Geophys. Res. Lett., 36, L19105
Soon, W., Baliunas, S., Posmentier, E. S., & Okeke, P. 2000, New Astron., 4, 563
Steinolfson, R. S. 1985, ApJ, 295, 213
Stenflo, J. O. 1994, in Solar Surface Magnetism, eds. R. J. Rutten, & C. J. Schrijver, NATO Adv. Study Inst. (ASI) Ser. C, 433, 365
Stucki, K., Solanki, S. K., Schühle, U., et al. 2000, A&A, 363, 1145
Stucki, K., Solanki, S. K., Pike, C. D., et al. 2002, A&A, 381, 653
Telloni, D., Zank, G. P., Stangalini, M., et al. 2022, ApJ, 936, L25
Terradas, J., Soler, R., Oliver, R., et al. 2022, A&A, 660, A136
Timothy, A. F., Krieger, A. S., & Vaiana, G. S. 1975, Sol. Phys., 42, 135
Tripathi, D., Chakrabarty, D., Nandi, A., et al. 2023, in The Era of Multi-Messenger Solar Physics, eds. G. Cauzzi, & A. Tritschler, Proc. IAU Symp., 372, 17
Tu, C. Y., & Marsch, E. 1995, Space Sci. Rev., 73, 1
Tu, C. Y., Pu, Z. Y., & Wei, F. S. 1984, J. Geophys. Res., 89, 9695
Tu, C. Y., Marsch, E., Wilhelm, K., & Curdt, W. 1998, ApJ, 503, 475
Tu, C.-Y., Zhou, C., Marsch, E., et al. 2005, Science, 308, 519
Tulasi Ram, S., Liu, C. H., & Su, S. Y. 2010, J. Geophys. Res.: Space Phys., 115, A12340
Vainio, R., Laitinen, T., & Fichtner, H. 2003, A&A, 407, 713
Verbanac, G., Vršnak, B., Veronig, A., & Temmer, M. 2011, A&A, 526, A20
Vršnak, B., Temmer, M., & Veronig, A. M. 2007, Sol. Phys., 240, 315
Wagner, W. J. 1975, ApJ, 198, L141
Wagner, W. J. 1976, in Basic Mechanisms of Solar Activity, eds. V. Bumba, & J. Kleczek, IAU Symp., 71, 41
Wang, Y. M. 2009, in The Origin and Dynamics of Solar Magnetism, eds. M. J. Thompson, A. Balogh, J. L. Culhane, et al. (Springer), 32, 383
Warren, H. P., Mariska, J. T., & Wilhelm, K. 1997, ApJ, 490, L187
Webb, D. F., & Davis, J. M. 1985, Sol. Phys., 102, 177
Wiegelmann, T., Thalmann, J. K., & Solanki, S. K. 2014, A&Arv, 22, 78
Wilhelm, K. 2006, A&A, 455, 697
Wilhelm, K. 2012, Space Sci. Rev., 172, 57
Wilhelm, K., Marsch, E., Dwivedi, B. N., et al. 1998, ApJ, 500, 1023
Xia, L. D., Marsch, E., & Wilhelm, K. 2004, A&A, 424, 1025
Yang, S. H., Zhang, J., Jin, C. L., Li, L. P., & Duan, H. Y. 2009, A&A, 501, 745
Younas, W., Khan, M., Amory-Mazaudier, C., & Amaechi, P. O. 2022, Space Weather, 20, e2022SW003176
Zhang, J., Zhou, G., Wang, J., & Wang, H. 2007, ApJ, 655, L113
Zirker, J. B. 1977, Rev. Geophys. Space Phys., 15, 257